

AKARI Far-Infrared Source Counts in the Lockman Hole

Shuji MATSUURA¹ Mai SHIRAHATA¹ Mitsunobu KAWADA² Yasuo DOI³ Takao NAKAGAWA¹
 Hiroshi SHIBAI² Chris P. PEARSON¹ Toshinobu TAKAGI¹ Woong-Seob JEONG¹ Shinki
 OYABU¹ and Hideo MATSUHARA¹

¹*Department of Infrared Astrophysics, Institute of Space and Astronautical Science (ISAS), Japan
 Aerospace Exploration Agency (JAXA) 3-1-1, Yoshinodai, Sagamihara, Kanagawa 229-8510, Japan
 matsuura@ir.isas.jaxa.jp*

²*Graduate School of Sciences, Nagoya University, Furo-cho, Chikusa-ku, Nagoya 464-8602, Japan*

³*Department of General System Studies, Graduate School of Arts and Sciences, The University of
 Tokyo, 3-8-1 Komaba, Meguro-ku, Tokyo 153-8902, Japan*

(Received 2007 April 11; accepted 2007 0)

Abstract

We report initial results of far-infrared observations of the Lockman hole with Far-Infrared Surveyor (FIS) onboard the AKARI infrared satellite. On the basis of slow scan observations of a $0.6 \text{ deg} \times 1.2 \text{ deg}$ contiguous area, we obtained source number counts at 65, 90 and $140 \mu\text{m}$ down to 77, 26 and 194 mJy (3σ), respectively. The counts at 65 and $140 \mu\text{m}$ show good agreement with the Spitzer results. However, our $90 \mu\text{m}$ counts are clearly lower than the predicted counts by recent evolutionary models that fit the Spitzer counts in all the MIPS bands. Our $90 \mu\text{m}$ counts above 26 mJy account for about 7% of the cosmic background. These results provide strong constraints on the evolutionary scenario and suggest that the current models may require modifications.

Key words: cosmology:observation - galaxies:evolution - galaxies:starburst - infrared:galaxies

1. Introduction

One of the main scientific objectives of AKARI (Murakami et al. 2007) is to investigate the history of galaxy evolution by measuring thermal emissions from interstellar dust heated by the UV light from stars. Far-Infrared Surveyor (FIS) onboard AKARI with four photometric bands of 65, 90, 140 and $160 \mu\text{m}$ (Kawada et al. 2007) is designed to detect such dusty objects at wavelengths near the peak of the dust emission. Mapping observations with AKARI in

the slow scan mode provide 1–2 orders of magnitude higher sensitivity than that in the all sky survey mode with fast scan, and they are suitable for probing distant luminous infrared galaxies.

The IRAS mission has discovered the presence of luminous infrared galaxies in local universe (Neugebauer et al. 1984), and their number counts show an excess over the predicted counts for the non-evolution scenario (Hacking & Soifer 1991). Far-infrared deep surveys with Infrared Space Observatory (ISO) have confirmed the findings by IRAS at much deeper flux levels; faint galaxy counts at 90 and 170 μm show steep increase of the excess counts as flux levels become fainter (Kawara et al. 1998, Puget et al. 1999, Efstathiou et al. 2000, Linden-Vornle et al. 2000, Matsuhara et al. 2000, Dole et al. 2001, Rodighiero et al. 2003, Kawara et al. 2004). These ISO results have inspired us with insight for the link between local luminous infrared galaxies and galaxy formation in early epoch, and they have provided useful constraints on the galaxy evolution models. The Spitzer Space Telescope (Werner et al. 2004) with the Multiband Imaging Photometer for Spitzer (MIPS) (Rieke et al. 2004) provided the number counts at 24, 70 and 160 μm down to 1–2 orders of magnitude deeper fluxes than previously reached and strongly constrained the galaxy evolution models (Papovich et al. 2004, Dole et al. 2004, Frayer et al. 2006a). The Spitzer results in all MIPS bands are well fitted with phenomenological models that predict most of the faint galaxies lie at redshifts between 0.7 and 0.9 (Dole et al. 2003, Lagache et al. 2003, 2004). Their models reproduce a broad shape of the measured redshift distribution for the Spitzer 24 μm samples, but the models still show discrepancies in some details at high redshifts $z > 1.5$ (Perez-Gonzalez et al. 2005, Le Floch et al. 2005, Caputi et al. 2006). They suggest that some details of the discrepancies in the redshift distribution between observations and models may come from the field variance. Therefore, further study of galaxy modeling with large amount of galaxy samples is still required. AKARI will provide us important constraints because of its high statistics on unprecedented sensitivity levels over the whole sky. This first deep survey validates the AKARI great capabilities, and furthermore bring new constraints especially at 90 μm , where IRAS and ISO data at faint flux levels below 100 mJy are not accurate enough to provide tight constraints on the evolutionary models.

Recent advances in observational study in wide wavelength range from optical to millimeter-wave have shown that luminous infrared galaxies are minority in local universe but major building blocks of the high redshift universe in terms of the total radiation energy release (Blain et al. 2002). Unresolved faint galaxies at high redshifts would form the Cosmic Infrared Background (CIB). In fact, CIB in the far-infrared regime measured with COBE (COsmic Background Explorer) accounts about half of the total energy of optical/infrared background (Puget et al. 1996, Hauser et al. 1998, Lagache et al. 1999, Hauser & Dwek 2001, Finkbeiner et al. 2002). That tells us the importance of exploration of far-infrared sources which are responsible for the energy release in the cosmic history. Recent Spitzer results of ultra-deep

galaxy counts at $70\ \mu\text{m}$ (Frayer et al. 2006b) and of the stacking analysis for faint sources at 70 and $160\ \mu\text{m}$ accompanied with the $24\ \mu\text{m}$ sources (Dole et al. 2006) show that more than $\sim 70\%$ of CIB has been resolved into point sources. However, previous galaxy counts at the peak of the measured CIB ($\sim 100\ \mu\text{m}$) in between the MIPS bands have not reached to such deep levels.

In this work, we performed far-infrared deep surveys with AKARI in the Lockman hole, in order to measure the source counts at previously unexplored sensitivity near the photometric bands covering the peak wavelength of CIB. This survey has been done in the performance verification (PV) phase of AKARI mission to demonstrate and evaluate performance of the slow scan observation. The survey area was, therefore, limited to $0.7\ \text{deg}^2$, and east patch of the Lockman hole (LHEX field), where many observations including follow-up observations from the ground for the ISO survey (Oyabu et al. 2005, Rodighiero et al. 2005) have been done, was selected for the observation field so that the cross calibration between missions could be done. In this paper, we present the initial results of the number counts for the sources detected with AKARI.

2. Observations

The observations of the Lockman hole were carried out in the PV phase in 2006 May, to check the performance of the FIS instrument for observing faint objects and to demonstrate the slow-scan observations for wide-area mapping. The survey covers a $0.6\ \text{deg} \times 1.2\ \text{deg}$ ($0.7\ \text{deg}^2$) region centered at $\text{RA}(\text{J2000}) = 10^{\text{h}}52^{\text{m}}12^{\text{s}}$ and $\text{DEC}(\text{J2000}) = +57^\circ 18'00''$, the east side of the lowest cirrus region corresponding to the ISO deep survey.

The data were taken using the FIS-02 slow-scan observational mode of the astronomical observation template (AOT) with 15-arcsec/s scan rate and 2-s period reset (Kawada et al. 2007). The FIS-02 observation provides a map data with double sightings of each source in a 0.13-deg wide, 1.25-deg long strip area by a single turn-around scan. The mapping observation was carried out with 11 contiguous scans; 12 scans were actually done but one scan data were lost with trouble of the ground station. To secure sufficient redundancy and to improve the sensitivity, one third of the width of each single scan strip was overlapped with the next strip for producing mosaic image. It took 2 hours of telescope time in total to cover the entire survey field. The data in the four photometric bands, centered at $65\ \mu\text{m}$, $90\ \mu\text{m}$, $140\ \mu\text{m}$ and $160\ \mu\text{m}$, were simultaneously taken, and the same field was surveyed in all the bands except for a small margin of the survey area corresponding to the sight difference between field-of-view (FOV) of each band.

AOT includes the calibration sequence for each observation as follows. The dark measurements by closing the cold shutter and responsivity check with an internal calibrator are carried out during maneuver to change the satellite attitude from the all-sky survey mode to the source targeting mode. After the maneuver the shutter is opened, the sky signal is mon-

itored during a settling time for fine control of the satellite attitude, and then the slow-scan observation starts. At turning point of the round-trip scan, the shutter is shortly closed, and responsivity check with the internal calibrator is done. The total exposure time for the round-trip scan is 10 min. The same calibration sequence as above is repeated during the maneuver for returning to the all-sky survey mode. In addition to the calibration sequence by continuous light illumination, stimulator flashes every 1 min to check the responsivity drift is operated as is done in the all-sky survey mode. Such highly redundant calibration data set enabled us to correct the responsivity change referring the astronomical calibration data taken by separate observations with the same calibration sequence.

3. Data reduction and calibration

3.1. Initial reduction in time domain

The raw data were initially reduced using a part of the FIS All-sky survey pipeline tool for the ADU to volt conversion, flagging of bad data (cosmic-ray events and other discontinuities) and the correction of non-linear integration ramps. The reduced data were processed with an official data analysis tool specified for the FIS slow-scan observation (SS-tool) to produce the basic calibrated data products and the final co-added map.

Initial process of SS-tool is the slope calculation of the ramps removing the cosmic-ray events identified in each ramp and correcting the after effect of the calibration lamp (stimulator) flashes. The reset interval of the integration ramp for the Lockman hole observations is set to be 2 seconds. The 2-s ramps are comprised of 52 and 35 samples per pixel for 65/90 μm and 140/160 μm detectors, respectively. The slope calculation processing reduces the sampling rate to one data per ramp per array pixel to maximize signal-to-noise and to avoid a periodic structure arising from incompleteness of the non-linear ramp correction. For 15-arcsec/s scan, the reduced data provides only one data sample per pixel for a source crossing time, but the Nyquist sampling condition is resultantly satisfied in real space domain after co-addition of the data using all array pixels.

Glitches and subsequent tails induced by cosmic-ray hits affect the data severely because of slow transient behavior of the Ge:Ga detectors. The integration ramps affected by the glitches were flagged out, and the tails with a 20 s or a longer time constant were suppressed by median filtering in the background subtraction processing as described later. The tail with a short time constant is not filtered out in this stage, but the affected data are removed by the sigma clipping in the co-addition process. The stimulator flashes also causes after effects similar to the tails by cosmic-ray hits, but they were repeatable in amplitude and successfully corrected using a template of their average time profile with an accuracy limited by the random noise.

3.2. Flat fielding

The second step of the SS-tool processing is to produce basic calibrated data for each array pixel, i.e., the flat fielding. This process is based on the observations of known diffuse sources; zodiacal emissions and interstellar dust emissions, which are expected to be smooth within the field of view (FOV). The diffuse-source observations were used only for the flat fielding, and the absolute flux calibration for point-sources was separately done (see Section 4), because it might be different from that for diffuse-source due to complex aperture effects.

Zodiacal emissions are expected to be an almost perfect flat source; their anisotropy in arcmin scales are smaller than 1% (Abraham et al. 1998). At 65 and 90 μm , the sky brightness of the Lockman hole is dominated by the zodiacal emissions, and the contributions of Galactic cirrus (interstellar dust) emissions, bright point sources and CIB are expected to be negligible. Hence, observed sky itself could be used for the flat fielding. The responsivity distribution of the detector arrays is derived from the average of time series data during the slow scan, where the average was calculated after removing the data that exceeds the 3-sigma noise level for each pixel. The flat was built from the data during the first half of the single turn-around scan of each pointed observation, because the latter part of the data was affected by the stray light as described in the following section. The flat fielding is done by dividing the data by the responsivity distribution. With this "self" flat fielding method, any stripes in the image caused by the flat field error were buried under the random noise.

At 140 and 160 μm , detector signals are dominated by 'offset' light with a constant intensity from the internal light source. The offset light is implemented to improve response speed of the stressed Ge:Ga detector specified for fast scan of the all sky survey mode (more than 10 times faster than the slow scan used for the Lockman hole survey). Although Galactic cirrus emissions at high latitudes could be a flat source with moderate smoothness ($\sim 10\%$) and relatively high brightness, their signals are less than 10% of that of the offset light. Intensity distribution of the offset light at the aperture of detector arrays is estimated from the laboratory measurements to be uniform within 10%. Sky brightness towards the Lockman hole at 140 and 160 μm is less than $\sim 2\%$ of the offset light, and its fluctuation is also negligible. Hence, the self flat fielding method with the average sky signal including the offset light was applied to correct the responsivity variation in the detector arrays, as was done for the 65 and 90 μm bands.

3.3. Subtraction of sky background

In order to emboss faint point-sources on the co-added map, subtraction of the sky background is required unless its brightness is constant in the field. Unexpectedly, there exists a stray light of earth limb emission onto the focal plane under a condition of small earth avoidance angles of the telescope, which varies with attitude and orbit of the satellite. The stray light shows not only a long-term variation depending on seasonal change of the orbital inclination but also short-term variation during a single observation due to change of the earth

avoidance angle at every moment. Brightness of the stray light has the maximum (2–3 MJy/sr at 90 μm) at the beginning and the end of the slow scan, and the minimum and plateau region appear around the mid time.

To subtract such slowly varying components as the stray light, we applied the median filtering to the data in time domain with a window size of 20 data samples corresponding to 10 arcmin (~ 15 times FWHM). Then, the smoothed component was subtracted from the data. As a result of this filtering, extended structure larger than roughly a half of the window size disappears from the map.

3.4. *Co-addition and position accuracy*

The final step of the SS-tool processing is the co-addition of the calibrated time series data onto a sky grid. The sky position of each data point was derived from the telescope boresight according to the satellite attitude and from the array pixel map on the focal plane. The grid pixel sizes for all the wave bands were set to 30 arcseconds to secure redundancy, i.e., sufficient number of data per pixel (>5 on the average). In the co-adding process, small glitches and other artifacts were sigma-clipped with the standard deviation calculated at each grid pixel. Threshold for the sigma-clipping was set to 1.5 times standard deviation. Percentage of the rejected data in this process was about 3% of the original data.

Co-addition of the data that were taken in different scans requires accurate sky position of each array pixel. The telescope boresight has been calibrated with the slow-scan observations of stars and asteroids, and the resultant position accuracy is approximately 10 arcseconds in absolute measure. The array pixel map is based on the optical simulation and its in-flight confirmation with point-source observations. The image distortion has not been fully measured in the entire FOV, but the in-flight measurements at limited positions have been carried out with observations of point sources including a bright source in the field. As a result of the measurements, the simulation has been verified with an accuracy of 10 arcseconds, which is limited by the absolute position accuracy.

3.5. *Final co-added maps*

In Fig. 1, we show the final co-added maps of the Lockman hole field at all wavelengths in equatorial coordinates with a pixel size of 30 arcseconds. The image after Gaussian smoothing with a window size of 1 arcminute is shown as linear contours in the unit of surface brightness. The pixel noise of each map was computed and summarized in the last column of Table 1 in surface brightness. At 65, 140 and 160 μm , the pixel noises are dominated by instrumental noise. At 90 μm , the pixel noise is contributed by the source noise, which can be recognized as a positive tail exceeding the standard deviation in the histogram of pixel distribution. The noise difference between the 65 and 90 μm data arises from differences in optical efficiency and filter bandwidth, while the detectors for these two bands are identical. The noise values for the 140 and 160 μm bands are different for the same reason. Consequently, the 90 μm band is the

most sensitive in all the photometric bands.

4. Photometry and point-source calibration

4.1. Source extraction

To extract point sources from the final co-added image, we used photometry tools, FIND, GCNTRD and APER, in the IDL Astronomy User's Library at NASA/GSFC (Landsman 1993). The tools search center positions of point sources with a Gaussian window function approximating the Point Spread Function (PSF) and measure the fluxes by aperture photometry. PSF in each wavelength band is derived from many observations in the PV phase and for calibration. The aperture radius was set to the full width half maximum (FWHM) of PSF. The aperture photometry was carried out without the sky subtraction, which was already done in the median filtering process. This sky subtraction method is helpful to avoid losing sources near a defect pixel caused by some artifacts.

4.2. Photometric calibration

Photometric calibration used in this paper is based on point-source observations in the PV phase in various fields, because of lack of well-calibrated source in the Lockman hole. According to the measured PSF, the photometric signals were compared with the expected fluxes of the calibration sources converted to the 'flat' spectra, $\nu \times F_\nu = \text{constant}$, and their linear correlation factors were derived. The expected fluxes of the calibration sources range from 2 Jy to 200 Jy at 90 μm , and deviation from the linear relation had no flux dependence in such a wide flux range. The calibration accuracy estimated from the standard deviation for various measurements was 17%, 16%, 12% and 22% at 65, 90, 140 and 160 μm , respectively. The point-source noise in flux unit, i.e. the 1-sigma detection limit for point source, is derived from the pixel noise in surface brightness and the aperture correction factor, as summarized in Table 1.

4.3. Color uncertainty

As the flux calibration for AKARI refers to the flat spectrum, the real flux is obtained by the color correction depending on Spectral Energy Distribution (SED) of the source. However, it is difficult to measure the infrared color for all the detected sources especially at faint flux levels, because most of the sources were detected at 90 μm only. Hence, for producing the source counts we assume that SED of all sources have the flat spectrum, and we estimate the uncertainties of fluxes for various SEDs.

The color correction was available only for bright sources detected in multiple wavelength bands of AKARI. In Fig. 2, color-corrected (open symbols) and uncorrected (filled symbols) spectra of three bright sources in the Lockman hole are shown. The data are compared with modified graybody spectra with different color temperatures; combinations of a graybody spec-

trum with an emissivity β , $F \sim \nu^\beta \times B(T)$, and natural extension from the graybody towards shorter wavelengths by a power-law spectrum with an index α , $F \sim \nu^{-\alpha}$, (e.g., Blain et al. 2002). The error bars are the point-source noise in Table 1. These sources have been detected by the ISO survey and optically identified, and their redshifts have been measured by spectroscopic observations (Oyabu et al. 2005). Two of the sources, ID76 and ID87, are nearby star-forming galaxies at $z = 0.08$ and 0.09 , and the color correction is up to 10% in all bands. The modified graybody models ($T=27$ K, $\beta=1.5$ and $\alpha=2.4$ for ID76, $T=23$ K, $\beta=1.5$ and $\alpha=2.4$ for ID87) give good fits to the measured spectra even for uncorrected data. Another source (ID104) is ULIRG with a moderate redshift of $z = 0.362$. A graybody model with $T=25$ K (effectively $T=18$ K corresponding to the redshift), $\beta=1$ and no power-law component provides reasonable fit to the data. The color correction for the $65 \mu\text{m}$ data is 29%, which is an extreme case in the parameter range of color temperature. If the assumed color for ID104 is correct, the real $65 \mu\text{m}$ flux is expected to be below the detection limit, but the observed flux shows a finite value at $65 \mu\text{m}$. The high flux at $65 \mu\text{m}$ may be due to noise-induced flux boosting, which is similar to Eddington bias or Malmquist bias and usually seen for sources near the detection limit (Heraudeau et al. 2004).

Frayer et al. (2006a) reported that the Spitzer sources detected at 24, 70 and $160 \mu\text{m}$ in the xFLS field have a typical dust temperature of 30 K with an emissivity of $\beta=1.5$ and a power-law index of $\alpha=2.4$. This color temperature is consistent with 15–25 K for $\beta=2$ derived from the European Large Area ISO Survey (ELAIS) (Heraudeau et al. 2004) and from the ISO deep survey in Lockman hole (Oyabu et al. 2005). According to these results, most of far-infrared sources have color temperatures ranging from 15–40K with $\beta=1$ –2 and of the power-law indices of $\alpha=1$ –2.5. Uncertainty of the flux measurement for the sources with colors in this parameter range is estimated to $+4/-38\%$, $+15/-6\%$, $+9/-4\%$ and $+2/-1\%$ at 65, 90, 140 and $160 \mu\text{m}$, respectively. In most cases for high temperature sources, the color correction uncertainties are smaller than the flux calibration errors. For nearby cold dust components or high redshift sources, the uncorrected flux at $65 \mu\text{m}$ assuming the flat spectrum could be greatly overestimated.

5. Source counts

5.1. $90 \mu\text{m}$ counts

The final catalogs were first produced at $90 \mu\text{m}$, at which the deepest data were obtained. Sources with signal-to-noise ratios of $S/N > 3$ were extracted according to the point-source noise shown in Table 1, while a sharp decrease in number counts due to the incompleteness appeared at $S/N \sim 1.8$ (16 mJy). At $90 \mu\text{m}$, 85 sources were found in the entire survey field down to 26 mJy. The surface density of sources derived from the beam size, $\Omega = 4.5 \times 10^{-8}$ sr, is ~ 70 beams per source. This is far above 22 beams per source that is required for the 90% completeness

without source confusion estimated by Helou & Beichman (1990) and also much greater than 27 beams per source as a criterion for the 3-sigma detection in case of the Euclidian counts (Franceschini 2000).

In Fig. 3 the integral counts at 90 μm are plotted as filled circles. The data are raw counts not corrected for incompleteness. Error bars along the count axis are 1-sigma Poisson uncertainty, and the flux errors correspond to total uncertainties including both absolute calibration and color correction. Our results are compared with those from the ISO surveys at 90 μm towards the Lockman hole (Linden-Vornle et al. 2000, Kawara et al. 2004, Rodighiero et al. 2003) and the ELAIS field (Heraudeau et al. 2004). A no-evolution model by Pearson (2007) is also shown as a reference.

Our source counts in the Lockman hole reaching to ~ 25 mJy at $S/N > 3$ are roughly two times deeper than those of ISO surveys. Hence, it is not easy to compare our data with previous results at the faint end. At shallower flux levels our data can be directly compared with the ISO results, because a large part of our survey area is overlapped with the ISO observed field. At ~ 100 mJy, our counts show good agreement with all the ISO results except for Kawara et al. (2004). A small discrepancy at the bright end could be due to large statistical errors of our counts.

At fainter flux levels, our integral counts seem to agree with Rodighiero et al. (2003) at 60 and 30 mJy. However, individual sources in the counts listed in Rodighiero et al. (2003) are not always consistent with our measurements in both flux and position, while relative fluxes of all the sources listed in Kawara et al. (2004) are well aligned with our data, as described in Appendix. Our counts do not show the strong excess reported in Kawara et al. (2004) and also in related papers (Kawara et al. 1998, Matsuhara et al. 2000). This discrepancy is partly explained by different flux calibration by a factor of ~ 2 (see Appendix). Simple linear scaling of their data to ours can be reasonably done at fluxes brighter than 100 mJy, but it fails at fainter levels because of steep rise of their counts. In spite that the ISO results by Rodighiero et al. (2003) and Kawara et al. (2004) in the Lockman hole were derived from the same data set, their results show large difference with each other. This fact suggests the difficulty in reduction of the ISO 90 μm data; they have suffered from glitches and tails induced by cosmic rays (Franceschini et al. 2001).

In order to check the effect of the field variance to the counts, we divided our observed field into two at $\text{DEC} = 57.28$ deg as number of the detected sources for the two sub-samples are equal to each other, and then we produced the source counts for each sub-samples. In Fig. 3 the source counts in the fields of $\text{DEC} < 57.28$ deg and $\text{DEC} > 57.28$ deg are plotted as dashed and dotted lines, respectively. It is clear that at brighter flux levels the lower DEC field contains about twice more sources than the higher DEC field, while at the faint end the counts in the two fields agree with each other. The field variance for this case is significant exceeding the Poisson uncertainty.

In Fig. 4 the same 90 μm counts are shown in differential form dN/dS normalized to the Euclidean law $N \sim S^{-2.5}$ with error bars of 1-sigma Poisson uncertainty. Total uncertainty of absolute calibration and color correction is indicated with a cross symbol at lower left (at 20 mJy) of the figure. The results are summarized in Table 2 together with the integral count data. Our differential counts are compared with previous results from the same references as the integral counts. Again, our counts are slightly lower than that for the previous observations, but both the ISO results except for Kawara et al. (2004) and our results show a general tendency of flat counts with no steep rise or drop in the measured flux range.

5.2. Counts at other wavelengths

At wavelengths other than 90 μm , the sources accompanied with the 90- μm sources were selectively extracted. In terms of real source extraction against any artifacts, the catalog produced in such a way is more reliable than that individually produced at each wavelength. The 90- μm selected catalogs are possibly biased as to miss exceptionally hot or cold/high- z populations. However, such biasing effects are expected to be small. Because, the detection limit at 90 μm is much better than that at the other wavelengths, and any detected source having ordinary temperatures of $T=15\text{--}40\text{K}$ with $\beta=1\text{--}2$ should be identified at 90 μm .

To extract the commonly detected sources, a centroid near a 90- μm source was searched at each wavelength allowing a small position difference corresponding to the beam size. Only signals associated with the 90 μm sources having $S/N > 5$ were regarded as real sources. At 140 μm , the signal-to-noise threshold for the source extraction was lowered to $S/N > 2.5$ to secure statistically significant number of samples, while the threshold at 65 μm is set to $S/N > 3$. The signals rejected by this criteria showed relatively large position differences from the 90 μm sources compared with the real sources. As a result, 11 and 6 sources were found at 65 and 140 μm , respectively. It is noteworthy that all the 6 sources at 140 μm were identified at 65 μm . At 160 μm , no signal matches to the criteria for source extraction.

In Fig. 5 and Fig. 6, differential source counts at 65 and 140 μm are plotted with filled circles. Error bars for the counts are 1-sigma Poisson uncertainty. The flux error corresponding to both absolute calibration error and color correction uncertainty are shown by a cross symbol in each figure. Our results are compared with Spitzer counts at 70 and 160 μm , respectively, in GTO fields (Dole et al. 2004) and xFLS field (Frayser et al. 2006a). The Spitzer data were converted at 65 μm and 140 μm with a flat spectrum of $\nu \times F_\nu = \text{const}$ as assumed in their paper. The Spitzer GTO data in the intermediate flux range show a field variance between those taken in two different fields (Marano and CDFS; Chandra Deep Field South). At both wavelengths, our counts are slightly higher than the Spitzer counts but agree with them within error bars and the field variance.

In Fig. 4, partial number counts for the 90 μm sources that are constituents of the 65 μm counts are plotted with an open circle. About half of the 90 μm counts in a range from

70 to 160 mJy consists of the 65 μm sources. The average color temperature of these sources without color correction is $T \sim 40$ K for $\beta=1.5$, corresponding to the color ratio $S_{90}/S_{65} \sim 1$. This temperature is hotter than that of the Spitzer sources in the xFLS field, $T \sim 30$ K for $\beta=1.5$ (Frayser et al. 2006a). The main reason that our 65 μm counts are slightly higher than the Spitzer counts is the field variance; most of the 65 μm sources lie in the lower DEC field where more bright sources exist, as described in section 5.1. Note that our 140 μm counts are also consistently higher than the Spitzer 160 μm counts. The remained half sources in the 90 μm counts would have lower color temperatures as $T < 30$ K to be consistent with the Spitzer results. Such redder color populations may contribute to the 65 μm counts at fluxes below the detection limit.

6. Discussions

As described in the last section, our source counts at 65 and 140 μm are fairly consistent with Spitzer observations. In this sense, our count data at 90 μm , which lie in between 65 and 140 μm , are simply expected to agree with recent evolutionary models that show excellent agreement with the Spitzer counts. In the following, we describe the comparison of our counts with the models.

In Fig. 4, 5 and 6, source counts predicted from models at each wavelength are shown; dashed: Pearson (2007) and dash-dotted: Lagache et al. (2003, 2004). In Fig. 4, Lagache et al. (2003) model taken from Heraudeau et al. (2004) was used, because the model counts at the wavelength near 90 μm is not presented in Lagache et al. (2004), but the difference between their models of 2003 and 2004 are negligible in the AKARI wavelength bands (Lagache et al. 2004). For Fig. 5 and 6, the predicted counts at 70 and 160 μm in Lagache et al. (2004) were converted to 65 and 140 μm , respectively, assuming the flat spectrum. A non-evolution model by Pearson (2007) is also shown as a reference. Lagache et al. (2003, 2004) uses phenomenological approach aiming to build the simplest model. They assume that infrared galaxies are mostly powered by starformation and use typical SEDs of normal and starburst galaxies. The luminosity function is represented by these two activity types. The model parameters are adjusted to fit the number counts in multi-wavelength bands from mid-infrared to sub-mm, the redshift distributions, the local luminosity functions at 60 and 850 μm , and CIB. The contemporary galaxy evolution model of Pearson (2007) uses a backward evolution process based on the IRAS all-sky PSCz multi-component luminosity function defined at 60 μm comprising of cool normal quiescent galaxies, and a warmer component defined by infrared luminosity as $L_{IR} < 10^{11} L_{\odot}$ starburst galaxies, $L_{IR} > 10^{11} L_{\odot}$ LIRG sources, $L_{IR} > 10^{12} L_{\odot}$ ULIRG sources and AGN. Both luminosity evolution and density evolution is included in the models. This model fits the observed source counts from the 2–1200 μm from the IRAS, ISO, Spitzer missions and the SCUBA/JCMT, MAMBO/IRAM instruments. Differences between these models are small at brighter fluxes, but at flux levels below 100 mJy strong evolution

effects set in and significant differences between models appear.

A significant result of the model comparison is that the observed counts at $90\ \mu\text{m}$ in a flux range of 26–160 mJy are apparently lower than the predicted counts using a model by Lagache et al. (2003, 2004), which show excellent agreement with Spitzer counts in all MIPS bands of 24, 70 and $160\ \mu\text{m}$ and also with our data at 65 and $140\ \mu\text{m}$, as shown in Fig. 5 and 6. Discrepancy between the model and data is clear at fainter levels; the model continues to increase while the observed counts keep constant. The model by Pearson et al. (2007) shows better fit with our $90\ \mu\text{m}$ counts, but it still predicts slightly too high counts to fit the data. Other models, e.g. Chary and Elbaz (2001), King and Rowan-Robinson (2003), and Balland, Devriendt and Silk (2003), also reproduce various observables including the source counts for the infrared luminous galaxies within uncertainties of the observation data, and all of them predict similar counts to above two models. Consequently, no model to explain the low $90\ \mu\text{m}$ counts is currently available.

The incompleteness of our data might lower the $90\ \mu\text{m}$ counts at fainter flux levels, but it is unlikely, because the 65 and $140\ \mu\text{m}$ counts derived from the $90\ \mu\text{m}$ selected catalogs are consistent with or even higher than the Spitzer data and the models. Separation between models and data starts already at ~ 80 mJy, where the signal-to-noise is high ($S/N \sim 10$) enough not to lose many sources. If the discrepancy is due to the flux calibration, our flux calibration has to be different by a factor of ~ 2 , which is unreasonably larger than our estimate of the calibration error. In order to explain our results, the evolutionary models may require some modifications.

It should be emphasized that our results provide strong constraints on the evolutionary scenarios. A new model to explain our results may be based on more complicated SEDs than previously used; faint galaxies may have exceptionally low emissivity at $90\ \mu\text{m}$ due to dust properties. There also exists a room to tune model parameters to represent high redshift components (e.g. ULIRG), because their redshifts and SEDs are not well defined. In any cases, the AKARI observations of much larger number of SED samples are essential for constructing the new model. Combination of source counts and redshift distributions are much stronger discriminators for various evolutionary models (e.g. Le Floc'h et al. 2005). Although the redshift measurements by optical spectroscopy for some of the ISO $90\ \mu\text{m}$ sources have been done (Oyabu et al. 2005, Rodighiero et al. 2005), only 9 spectroscopic samples in their catalogs match with the AKARI $90\ \mu\text{m}$ sources. In the spectroscopic samples, 8 sources have redshifts of $z < 0.4$, and the remaining 1 source is $z = 1.1$. Such statistically poor samples with low redshifts cannot constrain any evolutionary models. Further measurements and analysis of the redshift distribution of the AKARI $90\ \mu\text{m}$ sources are required.

Unresolved sources below the detection limit form the CIB. The integrated flux of our $90\ \mu\text{m}$ counts down to 26 mJy corresponds to the surface brightness of 0.021 MJy/sr. This is only $\sim 7\%$ of the CIB estimated by Lagache et al. (2003) and Dole et al. (2006). Dole et al.

(2004) reported that the Spitzer counts in the GTO field at 70 and 160 μm down to 15 and 50 mJy account for about 23% and 7% of the CIB, respectively. For the xFLS survey down to 8 and 50 mJy, approximately 35% and 15% of the CIB were resolved at 70 and 160 μm , respectively (Frayser et al. 2006a). Frayer et al. (2006b) also claimed that ultra-deep Spitzer counts down to 1.2 mJy account for about 60% of the CIB at 70 μm and that a turn-over of the differential counts, as seen in the Spitzer 24 μm counts (Papovich et al. 2004), appears at ~ 10 mJy. If we simply assume the flat spectra for all galaxies, the turn-over point of the 90 μm counts is expected to be ~ 13 mJy. These results suggest that number of the bulk galaxies of the CIB lying below the point-source detection limit at 90 μm may steeply increase towards the turn-over point. In order to search for such missing sources, much deeper survey at 90 μm is demanded. The flux limit of the present survey is still above the confusion limit, and source counts to deeper levels can be obtained by spending much exposure time.

7. Conclusions

We presented far-infrared observations of the Lockman hole with AKARI satellite. In the performance verification phase, we performed slow scan observations in a $0.6 \text{ deg} \times 1.2 \text{ deg}$ contiguous area overlapping with the ISO survey field and obtained number counts of galaxies down to 77, 26 and 194 mJy (3σ) at 65, 90 and 140 μm , respectively. The counts at 90 μm are ~ 2 times deeper than previous measurements with ISO. Our results show that some of the ISO results should be reconsidered as described in Appendix.

Our 90 μm counts were several times lower than the predicted counts by recent evolutionary models that show good agreement with the Spitzer/MIPS data. On the contrary, the observed counts at 65 and 140 μm are consistent with previous measurements with Spitzer at 70 and 160 μm . Our 90 μm counts above 26 mJy accounts for $\sim 6\%$ of the CIB, and the bulk galaxies of the CIB may cause a steep rise of the counts below the detection limit. These results provide strong constraints on the evolutionary models.

The source counts presented in this paper were not color-corrected, because limited samples were available to examine the infrared colors of galaxies. Further study of the source counts could be done by proper color correction based on the measured SED of each source. A far-infrared deep survey in the lowest cirrus region with an area of ~ 10 square degrees near the south ecliptic pole, as a part of AKARI deep survey programs (Matsuhara et al. 2006), is expected to provide us a large number of samples over 1000 sources down to ~ 20 mJy at 90 μm . Moreover, the AKARI all-sky survey will provide us extremely high statistics of galaxy samples onprecedented sensitivity levels over the whole sky. The data sets obtained by such large-area surveys are promising not only for producing the SED templates for various galaxy populations but also for extending the flux range of the source counts to much brighter levels than we obtained in this work.

The AKARI mission is operated by Japan Aerospace Exploration Agency (JAXA), Nagoya University, the University of Tokyo and National Astronomical Observatory Japan, European Space Agency (ESA), Imperial College London, University of Sussex, Open University (UK), University of Groningen / SRON (Netherlands), and Seoul National University (Korea). The far-infrared detectors were developed under collaboration with The National Institute of Information and Communications Technology (Japan). The authors would like thank all the AKARI project members for their intensive effort.

Appendix 1. Comparison with the ISO source catalogs in the Lockman hole

To confirm the flux calibration at lower flux levels, we compared the measured $90\ \mu\text{m}$ fluxes of relatively bright sources with the ISO data for the same sources in Fig. 7. The dot-dashed and dashed lines are the best-fit lines with linear coefficients (scaling factor) of 0.88 ± 0.12 for Rodighiero et al. (2005) and 2.09 ± 0.17 for Kawara et al. (2004), respectively. In terms of the absolute flux scale, the observed flux in Rodighiero et al. (2005) is consistent with ours within the calibration accuracy. However, relative deviation from the linear relation for Kawara et al. (2004), $0.17/2.09 = 0.08$, is smaller than that for Rodighiero et al. (2005), $0.12/0.88 = 0.14$, i.e., their relative calibration in the bright flux regime shows good agreement with ours.

A large difference between Kawara et al.’s count data and ours may arise from the fact that their absolute calibration relies on a single reference, IRAS F10507+5723, whose flux in the IRAS Faint Source Catalog (FSC) at $100\ \mu\text{m}$ (1.22 Jy) is perhaps overestimated. In fact, the flux of this source measured with AKARI is 0.56 ± 0.10 Jy at $90\ \mu\text{m}$ and lower than the IRAS flux by a factor of ~ 2 . This factor is in good agreement with the scaling factor between Kawara et al. (2004) and our measurements for the sources as described above. A tendency for the IRAS FSC to overestimate the flux is also pointed out by Heraudeau et al. (2004) in the data analysis for the ELAIS survey. Our recent result of the flux comparison between the AKARI all-sky survey data and the IRAS point source catalog (PSC) shows large scattering of the AKARI/IRAS flux ratio up to ~ 5 even for bright sources at fluxes greater than 10 Jy in the IRAS PSC (Jeong et al. 2007). This result suggests the difficulty of flux calibration with small number of samples of IRAS sources.

A large deviation from the linear relation between the measured flux in Rodighiero et al. (2005) and ours seems to be related to the fact that some sources in their catalog are missing in our map. In Fig. 8, sources listed in their paper are plotted on the AKARI $90\ \mu\text{m}$ map as background. Many of the sources in their catalog are not identified by AKARI and vice versa, though only bright sources are identified. Some of their sources were misidentified as faint sources detected by AKARI at $S/N < 3$ and this fact results in large deviations in Fig. 7. Accordingly, there is no reason that their counts at fainter flux levels agrees with ours.

References

- Abraham, P., Leinert, C., Acosta-Pulido, J., Schmidtbreick, L., & Lemke, D. 1998, in *The Universe as seen by ISO*, ed. P. Cox, & M. Kessler, ESA SP-427, 145
- Balland, C., Devriendt, J. E. G., & Silk, J. 2003, *MNRAS*, 343, 107
- Blain, A. W., Smail, I., Ivison, R. J., Kneib, J.-P., & Frayer, D. T. 2002, *Phys. Rep.*, 369, 111
- Blain, A. W., Barnard, V. E., & Chapman, S. C. 2003, *MNRAS*, 338, 733
- Caputi, K. I., et al. 2006, *ApJ*, 637, 727
- Chary, R. & Elbaz, D. 2001, *ApJ*, 556, 562
- Devriendt, J. E. G. & Guiderdoni, B. 2000, *A&A*, 363, 851
- Dole, H., et al. 2001, *A&A*, 372, 364
- Dole, H., Lagache, G., & Puget, J.-L. 2003, *ApJ*, 585, 617
- Dole, H., et al. 2004, *ApJS*, 154, 87
- Dole, H., et al. 2006, *A&A*, 451, 417
- Efstathiou, A., et al. 2000, *MNRAS*, 319, 1169
- Finkbeiner, D. P., Davis, M., & Schlegel, D. J. 2000, *ApJ*, 544, 81
- Frayer, D. T., et al. 2006a, *AJ*, 131, 250
- Frayer, D. T., et al. 2006b, *ApJ*, 647, L9
- Franceschini, A. 2000, in *Galaxies at High Redshifts, Proceedings of the XI Canary Islands Winter School of Astrophysics*, ed. I. Perez-Fournon, M. Balcells, F. Moreno-Insertis and F. Sanchez (Cambridge University Press)
- Franceschini, A., Aussel, H., Cesarsky, C. J., Elbaz, D., & Fadda, D. 2001, *A&A*, 378, 1
- Hacking, P. B., & Soifer, B. T. 1991, *ApJ*, 367, L49
- Hauser, M. G., et al. 1998, *ApJ*, 508, 25
- Hauser, M. G., & Dwek, E. 2001, *ARA&A*, 37, 249
- Helou, G., & Beichman, C. A. 1990, *Proc. 29th Liege International Astrophysical Colloquium From Ground-Based to Space-Borne Sub-mm Astronomy*, ESA SP-314, 117
- Heraudeau, Ph., et al. 2004, *MNRAS*, 354, 924
- Jeong, W.-S., et al. 2007, *PASJ*, this volume
- Kawada, M., et al. 2007, *PASJ*, this volume
- Kawara, K., et al. 1998, *A&A*, 336, L9
- Kawara, K., et al. 2004, *A&A*, 413, 843
- King, A. J. & Rowan-Robinson, M. 2003, *MNRAS*, 339, 260
- Lagache, G., Abergel, A., Boulanger, F. X., & Puget, J.-L. 1999, *A&A*, 344, 322
- Lagache, G., Dole, H., & Puget, J.-L. 2003, *MNRAS*, 338, L555
- Lagache, G., et al. 2004, *ApJS*, 154, 112
- Landsman, W.B. 1993, in *Astronomical Data Analysis Software and Systems II*, A.S.P. Conference Series, Vol. 52, ed. R. J. Hanisch, R. J. V. Brissenden, and Jeannette Barnes, p. 246.
- Le Floc'h, E., et al. 2005, *ApJ*, 632, 169
- Linden-Vornle, M. J. D., et al. 2000, *A&A*, 359, 51
- Matsuhara, H., et al. 2000, *A&A*, 361, 407
- Matsuhara, H., et al. 2006, *PASJ*, 58, 673

Murakami, H., et al. 2007, PASJ, this volume
 Neugebauer, G., et al. 1984, ApJ, 278, L1
 Oyabu, S., et al. 2005, AJ, 130, 2019
 Papovich, C., et al. 2004, ApJS, 154, 70
 Pearson, C. 2007, Adv. Space Res., in press
 Perez-Gonzalez, P. G., et al. 2005, ApJ, 630, 82
 Puget, J.-L., Abergel, A., Berbard, J. P., Boulanger, F., Burton, W. B., Desert, F.-X., & Hartmann, D. 1996, A&A, 308, L5
 Puget et, J.-L., et al. 1999, A&A, 345, 29
 Rieke, G. H., et al. 2004, ApJS, 154, 25
 Rodighiero, G., Lari, C., Franceschini, A., Gregnanin, A., & Fadda, D. 2003, MNRAS, 343, 1155
 Rodighiero, G., & Franceschini, A. 2004, A&A, 419, L55
 Rodighiero, G., Fadda, D., Franceschini, A., & Lari, C. 2005, MNRAS, 357, 449
 Werner, M. W., et al. 2004, ApJS, 154, 1

Table 1. Parameters for aperture photometry

Wavelength	Pixel size	Aperture radius	Net integration time	Point-source noise	Pixel noise
[μm]	[arcsec]	[arcsec]	per pix [s]	(1σ) [mJy]	(1σ) [MJy/sr]
65	30	37	12	26	0.20
90	30	39	12	9	0.06
140	50	58	20	76	0.39
160	50	61	20	288	0.60

Table 2. Integral and differential counts at 90 μm

Integral counts			Differential counts		
S	Number	$N(> S)$	Average S	bin width	$dN/dS \times S^{2.5}$
[Jy]		[sr^{-1}]	[Jy]	[Jy]	[$\text{sr}^{-1} \text{ Jy}^{1.5}$]
0.119	4	1.92 e4	0.140	0.042	$3.39 \text{ e3} \pm 1.70 \text{ e3}$
0.088	9	4.33 e4	0.104	0.031	$2.70 \text{ e3} \pm 1.21 \text{ e3}$
0.065	18	8.66 e4	0.077	0.023	$3.10 \text{ e3} \pm 1.03 \text{ e3}$
0.048	30	1.44 e5	0.057	0.017	$2.63 \text{ e3} \pm 0.76 \text{ e3}$
0.036	45	2.16 e5	0.042	0.013	$2.11 \text{ e3} \pm 0.54 \text{ e3}$
0.027	85	4.09 e5	0.031	0.009	$3.58 \text{ e3} \pm 0.57 \text{ e3}$

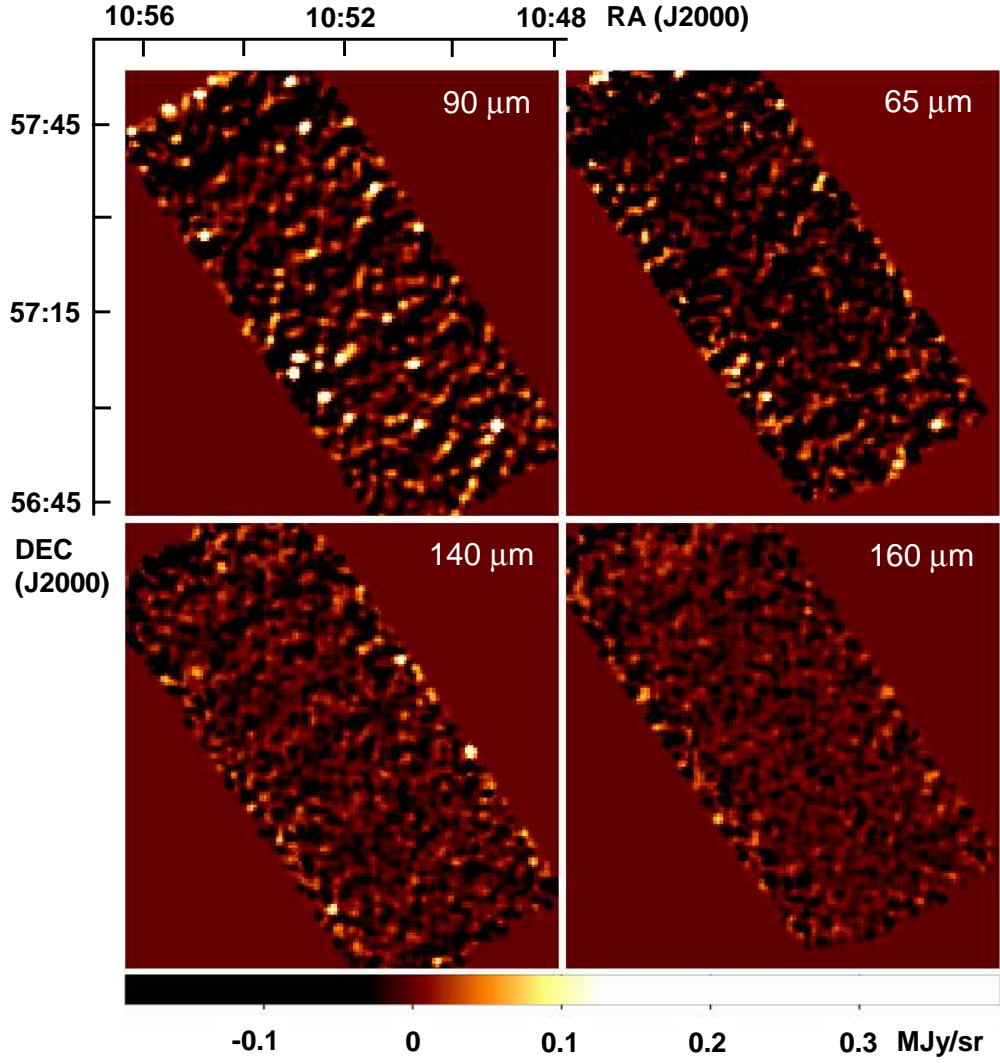


Fig. 1. The final co-added map of the Lockman hole field in all photometric bands in equatorial coordinates with the pixel size of 30 arcsec. Upper-left: 90 μm , Upper-right: 65 μm , Lower-left: 140 μm , and Lower-right: 160 μm . The image size is approximately 1.2 deg in RA \times 1.4 deg in DEC, and the observed area is 0.7 square degrees. Gaussian smooth filtering with a window size of 1 arcmin is applied to all images.

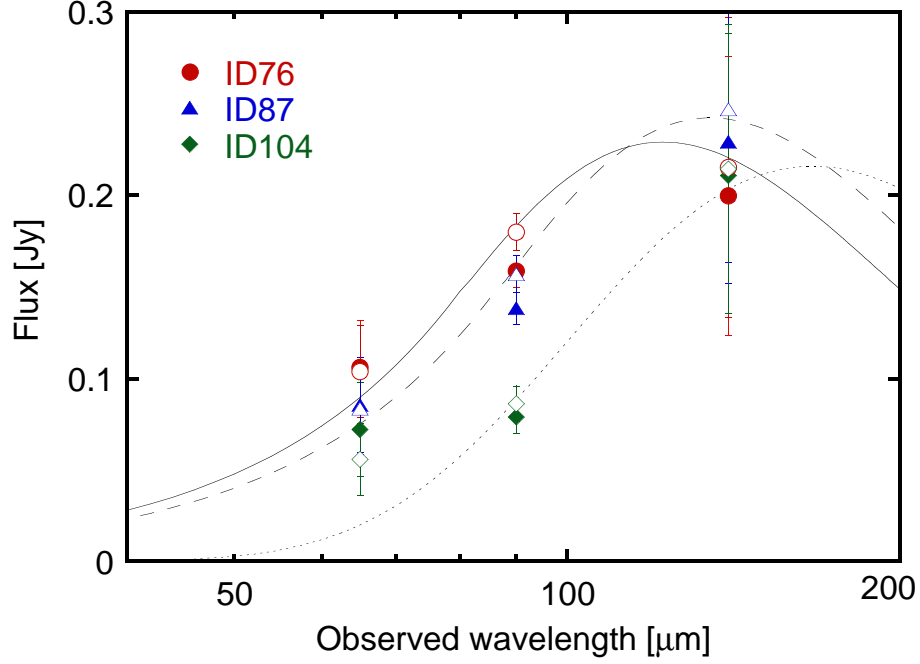


Fig. 2. Examples of the measured SEDs of bright sources in Lockman hole (ID76: circles, ID87: triangles and ID104: diamonds) as functions of the observed wavelength are compared with modified graybody spectra; $T=27$ K, $\beta=1.5$ and $\alpha=2.4$ for ID76 (thin line), $T=23$ K, $\beta=1.5$ and $\alpha=2.4$ for ID87 (dashed line), and $T=25$ K, $\beta=1$ with a redshift of $z=0.362$ (effectively $T=18$ K) for ID104 (dotted line). Filled and open symbols denote the data without and with the color correction, respectively. The model fluxes are scaled to fit the measured fluxes.

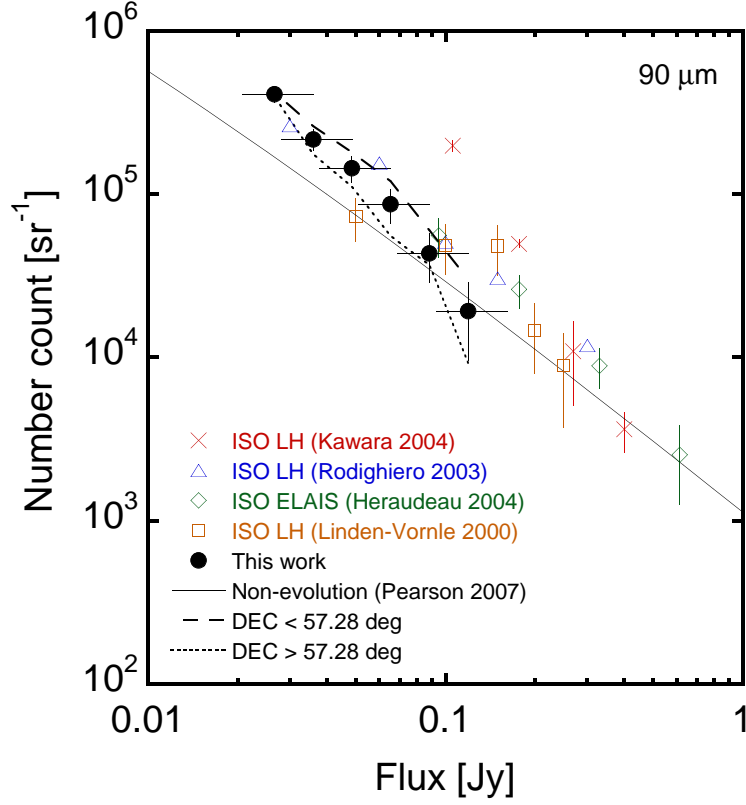


Fig. 3. Integral counts at $90\ \mu\text{m}$ with no correction for completeness (filled circles). Previous results of the ISO surveys at $90\ \mu\text{m}$ in the Lockman hole are shown; Linden-Vornle et al. 2000 (open squares), Kawara et al. 2004 (crosses), Rodighiero et al. 2004 (open triangles). The ISO counts in the ELAIS field (Heraudeau et al. 2004) are plotted with diamonds. The solid line is a non-evolution model by Pearson (2007). The dashed and dotted lines are the source counts for sub-samples in the fields of $\text{DEC} < 57.28\ \text{deg}$ and $\text{DEC} > 57.28\ \text{deg}$, respectively (see text).

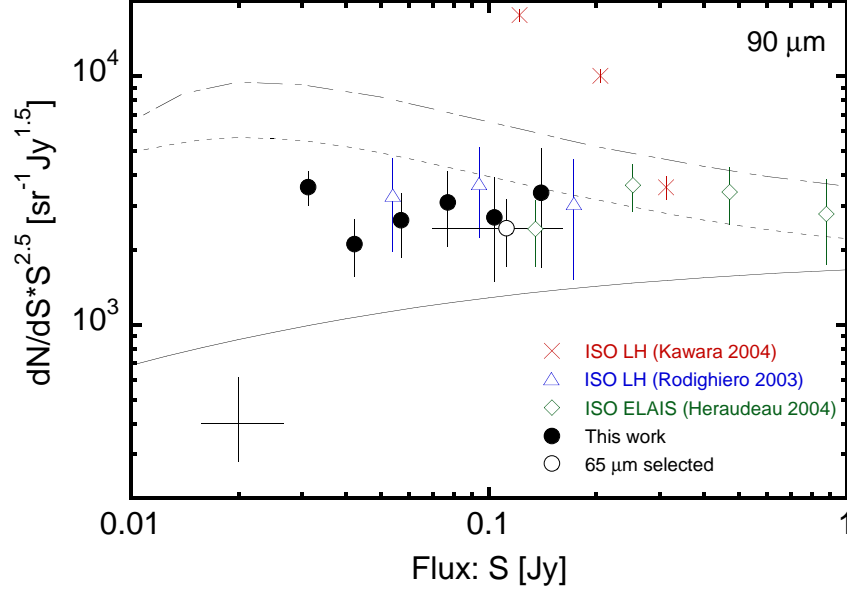


Fig. 4. Differential counts at $90\ \mu\text{m}$ with no correction for incompleteness. The ISO results are plotted with the same symbols as Fig. 3. A cross symbol at lower left shows total uncertainty including flux calibration error and color correction uncertainty (see text). Recent evolutionary models are also shown; solid and dashed lines: non-evolution and evolution model by Pearson (2007), and dash-dotted line: Lagache et al. (2003) taken from Heraudeau et al. (2004).

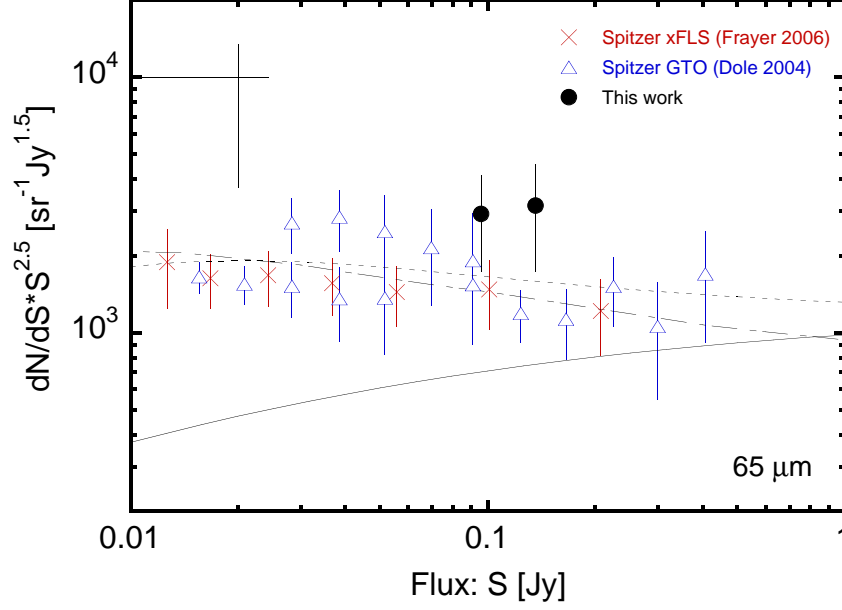


Fig. 5. Differential counts at 65 μm for the 90 μm selected sources (filled circles) compared with the Spitzer counts at 70 μm scaled to 65 μm (triangles: Dole et al. 2004, crosses: Frayer et al. 2006a). A cross symbol at upper left shows total uncertainty of the measured flux (see text). The evolutionary models same as Fig. 4 are also shown.

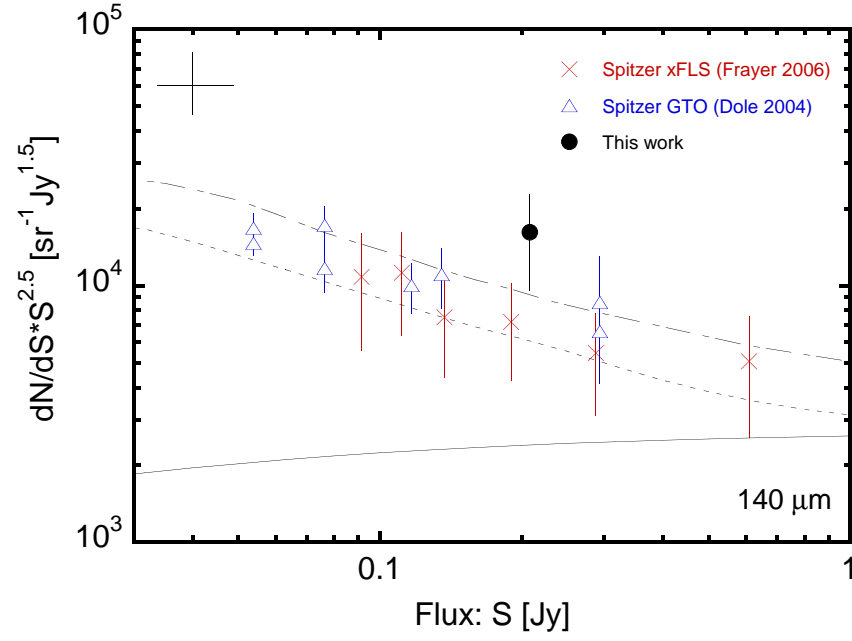


Fig. 6. Differential counts at 140 μm plotted with the same symbols as Fig. 5.

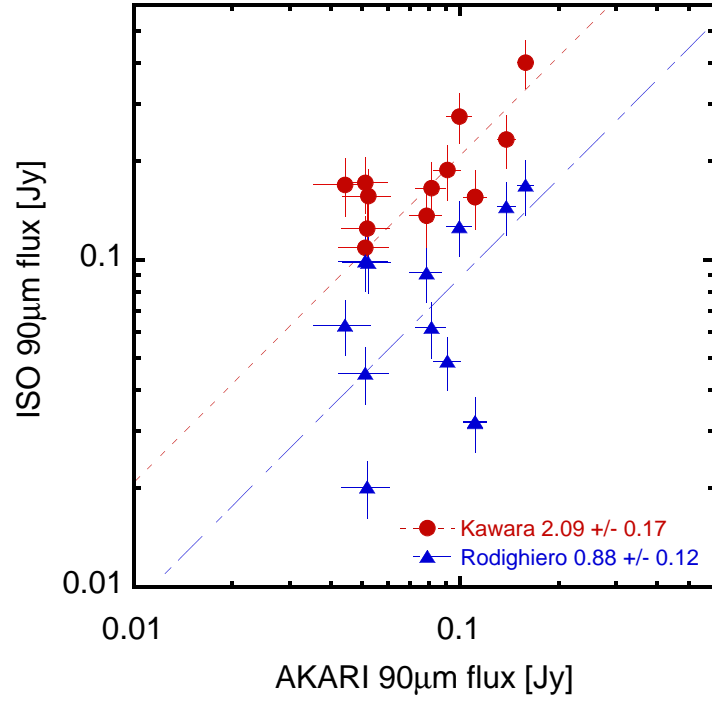


Fig. 7. Comparison of the AKARI measured flux for bright sources in the Lockman hole with ISO results (Kawara et al. 2004, Rodighiero et al. 2005).

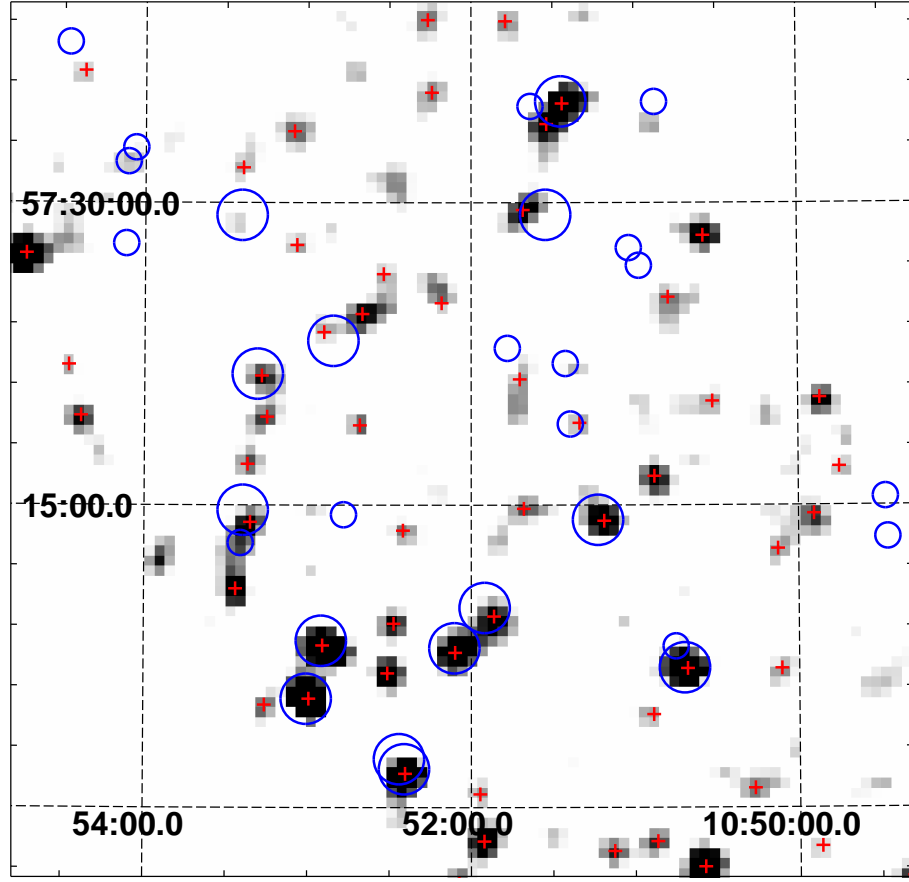


Fig. 8. Comparison of the source positions between Rodighiero et al. (2005) and this work (background contour). In this linear contour map, darker pixels have higher surface brightness as gray scale. Large circles denote brightest sources listed in the catalog of Rodighiero et al. (2005) and also in Oyabu et al. (2005). Small circles denote the remained faint sources in their catalog. Crosses are AKARI sources detected at $S/N > 3$. Many of the faint ISO sources are not identified by AKARI and vice versa. In Fig. 7, all the ISO sources identified by AKARI are plotted.